GSA Data Repository 2017058

Location, location, location: The variable lifespan of the Laramide orogeny

Copeland et al.

Methods

Palinspastic restoration. All points shown on Figs. 1 and 3 are displayed in their approximate locations at 25 Ma. Points not shown in their modern locations are those from the Basin and Range province, Baja California, and California (Fig. DR1). This reconstruction was achieved in seven steps: 1) Translation of Baja California (area in green in Fig. DR1) in a SSE direction so as to close the Gulf of California. 2) Translation of the area in California west of the San Andreas fault (black) SE-ward (parallel to the SAF) by 260 km (Crowell, 1962). 3) Squeezing of the Colorado extensional corridor (brown) in an E-W direction (holding the eastern margin fixed) by 15% (Howard and John, 1987; Davis and Lister, 1988). 4) Squeezing of the southern Basin and Range province of southern Arizona and southern New Mexico in an E-W direction (holding the eastern margin fixed) by 20% (Dickinson, 1991). 5) Squeezing of the Great Basin region (red) in an E-W direction (holding the eastern margin fixed) by 30% (Coney and Harms, 1984). 6) Translation of the modified Mojave desert region to the east such that it contacts the western portion of the modified southern Basin and Range region and the southern portion of the modified Great Basin region. 7) Rotation of points previously in eastern and northern California east of the San Andreas fault (purple and white, respectively) and the previously translated region originally west of the SAF (black) about a pole in southern California such that purple and white regions contacts the modified Great Basin region.

Line of projection. Collapsing the data in Fig. 1A onto a line to show the age-distance relationship is very much the treatment as presented in the classic paper by Coney and Reynolds (1977) however we think this updated version of this analysis offers three advantages over the original. Firstly, the presentation of Coney and Reynolds (1977) was based on a large proportion of K-Ar ages. This was what was available at the time but the intervening decades have produced a large number of U-Pb and $^{40}Ar/^{39}Ar$ ages, which are more reliable in estimating the time of formation of these rocks. Secondly, the data of Coney and Reynolds came mostly from New Mexico and Arizona but Fig. 1 shows data from a much broader area. Thirdly, the line of projection used by Coney and Reynolds was almost E-W in orientation but our line, with a bearing of about 045 (Fig. 1B), better approximates the vector of Farallon-North America convergence. The actual FA-NA direction of convergence varied from ~020 to 070 from 90 to 30 Ma (Saleeby, 2003; Yonkee and Weil, 2015) so 045 is the approximate average direction. Moreover, we find that for lines of projection with orientations from 045 to 055 the apparent rate of passage of the CSR and the apparent rate of the northwestward translation of the eastern edge of the Laramide deforming zone are closer to each other than for lines of projection with other orientations. Rates obtained using this line of projection may be less than the total convergence rate between FA and NA.

Numerical modeling. Our two-dimensional numerical model investigates subduction below the western United States from 90 to 30 Ma, using plate velocities and lithosphere structures consistent with those of the Farallon and North America Plates during this time. The modeling procedure follows that of Liu and Currie (2016). Plate convergence is imposed through boundary conditions and the oceanic plate geometry evolves dynamically within the model domain. The coupled thermal-mechanical evolution of the subduction zone is calculated with the finite-element code SOPALE (Fullsack, 1995). Arbitrary Lagrangian-Eulerian techniques are used to solve the equations of force balance, conservation of mass, and conservation of energy for incompressible creeping (Stokes) flow, assuming incompressibility and subject to plane-strain conditions and the assigned boundary conditions and material properties. The energy equation includes terms for strain heating and a temperature correction for adiabatic heating (Currie and Beaumont, 2011).

The model represents a vertical cross-section along profile A-A' (Figure 1), with the initial model geometry shown in Fig. DR2. The model domain is 4000 km wide and 900 km deep and consists of an oceanic plate that converges with a continental plate. The continental structure roughly reflects that of the western United States, with 120-km-thick lithosphere adjacent to the plate margin and 200-km-thick lithosphere inboard (Liu and Currie, 2016). The oceanic plate is 90 km thick and has a thermal structure consistent with a plate age greater 70 m.y (Yonkee and Weil, 2015). An oceanic plateau, representing the conjugate Shatsky Rise (CSR), is placed within the oceanic plate 600 km outboard of the plate boundary. The plateau has a crustal thickness of 24 km and is 1000 km long, similar to the general structure of the Shatsky Rise in the northwest Pacific (Korenaga and Sager, 2012; Zhang et al., 2016). The lithosphere thickness for the plateau region is the same as that for normal oceanic crust.

Table DR1 gives the mechanical and thermal properties for the materials in the model. All materials have a temperature-dependent density and a viscous-plastic rheology. The plastic rheology follows a Druker-Prager yield criterion, and the viscous rheology corresponds to thermally-activated power-law creep, with parameters taken from laboratory experiments. A scaling factor is used to linearly increase or decrease the viscous strength relative to the laboratory samples as a way to account for strength variations due to minor changes in composition or water content (Beaumont et al., 2006). Material parameters follow those used in previous studies (Liu and Currie, 2016; Beaumont et al., 2006). The sublithospheric mantle has a wet olivine dislocation creep rheology (Karato and Wu, 1993) to a depth of 660 km. Below this, the same flow law is used, and the effective viscosity is scaled upward by a factor of 5 to create a stronger lower mantle; we do not model the detailed phase changes within the mantle transition zone. The oceanic and continental mantle lithospheres are assumed to be relatively dry and thus their respective strengths are a factor of 5 and 10 times greater than the reference wet olivine. The larger factor for the continent reflects drier conditions that may be associated with cratonic lithosphere. For simplicity, the entire continental mantle lithosphere initially has the same viscous rheology.

Fig. DR2 shows the boundary conditions for the model domain. The top boundary is stress-free with a temperature of 0°C. The bottom boundary is a closed, free slip boundary with a temperature of 1657°C, corresponding to the mantle adiabat at 900 km depth. The side boundaries have no horizontal heat flux and no vertical slip. On the left boundary, oceanic lithosphere is introduced to the model domain at a prescribed rate (see below), and the incoming lithosphere has a prescribed temperature profile consistent with old (>70 m.y.) oceanic lithosphere. To maintain mass balance within the model domain, a uniform outflux is prescribed to the side boundaries of the sublithospheric mantle. Models are run in a continental reference frame by adding the continental velocity to all side boundaries (Liu and Currie, 2016).

The model is initialized with a 2D thermal structure that is consistent with the thermal boundary conditions and material properties, and the oceanic and continental plates are brought into isostatic equilibrium. Following this, subduction is initiated by applying a velocity of 5 cm/yr to the oceanic plate. After 600 km of convergence, a well-developed steep-angle subduction zone is created. At this time, the oceanic plateau is adjacent to the trench. We take this to represent a geological time of 90 Ma, in agreement with the inferred time of subduction of the CSR (Liu et al., 2010).

At this time, the plate velocities are modified to reflect the average margin-normal rates for the Farallon and North America plates from the Late Cretaceous to the Early Oligocene (Yonkee and Weil, 2015; Engebretson et al., 1984). From 90 Ma to 50 Ma, the oceanic and continental plates have velocities of 6 cm/yr and 4 cm/yr, respectively, resulting in a convergence rate of 10 cm/yr. Starting at ~55-50 Ma, there was a slow-down in plate convergence and North America westward motion (Yonkee and Weil, 2015; Engebretson et al., 1984). In the model, this is approximated by decreasing the convergence rate to 7 cm/yr from 50 Ma to 40 Ma (5 cm/yr oceanic plate; 2 cm/yr continental plate), and then 5 cm/yr from 40 Ma to 30 Ma (3 cm/yr oceanic plate; 2 cm/yr continental plate).

The model includes a phase change from basalt to eclogite for the oceanic crust and the CSR crust, using the phase diagram of Hacker et al. (2003). This phase change results in an increased crustal density; no other properties are changed. A density increase of 500 kg/m^3 is used, such that the eclogitized crust density is comparable to that observed in field studies (Austrheim et al., 1997) and it is 120 kg/m^3 more dense than mantle at the same temperature. The reaction kinetics of the basalt-eclogite phase change are not well-constrained and depend on factors such as temperature and hydration (van Hunen et al., 2002). Geological observations show that the phase change may occur sluggishly, with examples of metastable basalt at conditions well within the eclogite field (Hacker, 1996; Austrheim et al., 1997).

In the model, normal-thickness oceanic crust undergoes densification once its pressure-temperature conditions are within the eclogite stability field, following the procedure of Warren et al. (2008) to maintain mass balance in model. Model experiments show that a delay in densification of this material does not significantly affect the overall slab dynamics owing to the small thickness of this layer. On the other hand, the density of the CSR crust is the primary control on the development and removal of the flat slab segment. Previous geodynamic models show that basalt metastability is required in order for an oceanic plateau to remain buoyant enough to induce flat subduction (Liu and Currie, 2016; van Hunen et al., 2002; Arrial and Billen, 2013). In our model, the CSR basaltic remains metastable during subduction and it undergoes later densification, corresponding to a delayed eclogite phase change. Model experiments show that timing of the phase change—specifically, the time at which the plateau density exceeds that of mantle—controls the end of flat-slab subduction. Densification of the CSR crust is imposed from 58 to 48 Ma, assuming progressive eclogitization within the entire plateau crust. The timing of densification is chosen to match the geological observations (Figure 1B), and the duration is arbitrary but is consistent with the reaction rates from van Hunen et al. (2002). We speculate that the CSR crust was relatively water-poor and therefore the eclogite phase change was kinetically inhibited, allowing the crust to remain metastable after entering the eclogite stability field (Liu and Currie, 2016; Austrheim et al., 1997). The later onset of eclogitization may reflect the time at which there was sufficient water within the CSR crust to trigger the phase change. Dehydration reactions within the underlying oceanic mantle lithosphere (Currie and Beaumont, 2011) may provide the fluids for this.

Termination of flat subduction also requires that the flat-slab segment decouples from the continental mantle lithosphere and sinks. In our model, the continental mantle lithosphere is initially dry and thus is 10 times more viscous than the reference wet olivine under the same conditions. In order to allow decoupling and slab rollback, the continental mantle lithosphere must be weaker. Here, we assume that as the flat slab develops, fluids released from the slab infiltrate the continental mantle lithosphere, causing it to weaken (Karato and Wu, 1993). Currie and Beaumont (2011) show that extensive continental hydration could arise from the breakdown of hydrous minerals in the Farallon mantle lithosphere. Widespread hydration of the western US lithosphere is also indicated by geophysical observations (Humphreys et al., 2003). An alternate idea is that the western part of the continent was initially hydrated and thus weak owing to the long history of subduction prior to the Late Cretaceous. In the model, weakening occurs from 75 Ma until 50 Ma (i.e., during flat-slab subduction). Weakening occurs through a linear decrease in viscosity by an order of magnitude over this time, corresponding to a transition from a dry to wet mantle lithosphere. Weakening affects the region of the continent that overlies the flat slab. For simplicity, the entire thickness of mantle lithosphere is weakened, but flat slab removal only affects the deepest part of the lithosphere.

We note that our two-dimensional model is a simplified representation of the three-dimensional world. For example, with the plane-strain assumption, all material must flow within the model plane. Therefore, the model does not address the three-dimensional slab geometry (i.e., the along-strike transition between normal subduction and the flat-slab section) nor how along-strike mantle flow may affect the rate of slab shallowing or rollback (van Hunen et al., 2002; Arrial and Billen, 2013). Slab strength and material movement oblique to the model plane may affect the rate at which the slab geometry changes. In particular, rollback of the flat slab may be easier in three dimensions, as mantle can flow around the edge of the slab. In addition, plate convergence is imposed through assigned boundary velocities, whereas tectonic plates are driven by forces arising from density variations. Subduction of a buoyant plateau reduces the overall negative buoyancy of the slab, which may result in a decrease in the convergence rate (Arrial and Billen, 2013). Arrial and Billen (2013) argue that this effect is most important where the along-strike width of the plateau is a significant fraction of the subduction zone width. Saleeby (2003) and Liu et al. (2010) estimate that the along-strike width of the CSR was ~500 km, which is less than 10% of the length of the Cretaceous subduction zone of western North America. Therefore, we follow previous studies (van Hunen et al., 2002; Arrial and Billen, 2013) in assuming that continued plate convergence was driven mostly by forces acting on the slab to the north and south of the model profile, where no plateau was subducted.

An animation of our model is given in Movie DR1. In the plots, the CSR crust changes color as it enters the eclogite stability field, but as noted above, we assume that it remains metastable until 58 Ma. The model demonstrates how the development of flat-slab subduction is consistent with subduction of metastable, and thus buoyant, oceanic plateau crust. Removal of the flat slab commences at ~55 Ma, corresponding to the time at which the CSR crust density becomes greater than that of the mantle.

Data sources.

Data for igneous rocks were obtained from the North American Volcanic and Intrusive Rock Database (NAVDAT; http://www.navdat.org/) from all US western states, the Mexican states of Baja California Norte, Baja California Sur, Sonora, Chihuahua, and Coahuila, and the Canadian provinces of British Columbia and Alberta. Data were curated to remove duplicates and any ages not determined by the U-Pb zircon or $^{40}Ar/^{39}Ar$ methods. If U-Pb zircon data were available, we used that age. In the case where no U-Pb data were available and more than one $^{40}Ar/^{39}Ar$ age was reported, we used only the age from the mineral with the highest closure temperature for Ar.

Estimates for the time of youngest marine sedimentation are from stratigraphic descriptions of the various areas; sources for these estimates are given in Table DR2. Locations where a significant hiatus exists between the youngest marine strata and overlying non-marine were not included in the analysis.

Estimates for the timing of the initiation and the cessation of Laramide deformation come from a variety of data including stratigraphic, structural, thermochronologic, and geochemical observations. Structural data bracket the initiation or cessation of deformation by taking note of the age of deformed and undeformed rocks. Estimates of the age of deformation from stratigraphic data come from the age of the oldest strata for which isopachs suggest a Laramide depocenter adjacent to a Laramide uplift (Dickinson et al., 1988) and the presence of coarse-grained, non-marine sedimentation near a Laramide uplift (Dickinson et al., 1988; Cather, 2004), especially where conglomerate clasts indicate uplift and erosion of young pre-Laramide sedimentary units, possibly along steep basement-involved faults (Dickinson et al., 1988). Thermochronologic evidence is useful for determining when basement rocks were cooling rapidly. Evidence for an episode of rapid cooling does not necessarily mark the beginning of deformation. However, in some cases (e.g., Omar et al., 1994) it can be shown that the episode of rapid cooling was preceded by a long period of slow cooling. In such cases, the timing of acceleration of cooling can be reasonably ascribed to the initiation of shortening (or to a time slightly after the beginning of deformation). Sources and types of data for the initiation of deformation and the cessation of deformation are given in Tables DR3 and DR4, respectively.

Analysis of oxygen isotopes of pedogenic and lacustrine carbonates and hydrogen isotopes from volcanic rocks suggest that surface elevations during the early Cenozoic were at least 2 km, and in many cases 3 km above sea level. Sources for our presentation of these data in Fig. 1 are given in Table DR5.

Fig. DR3 is a map keyed to the sources given in Tables DR2-DR5.

REFERENCES

Arrial, P.-A., and Billen, M.I., 2013, Influence of geometry and eclogitization on oceanic plateau subduction, Earth Planet. Sci. Lett., v. 363, p. 34-43.

Austrheim, H., Eramberta, M., and Engvik, A.K., 1997, Processing of crust in the root of the Caledonian continental collision zone: the role of eclogitization, Tectonophys., v. 273, p. 129-153.

Ayers, W.B., Jr., 1986, Lacustrine and fluvial-deltaic depositional systems, Fort Union Formation (Paleocene), Powder River Basin, Wyoming and Montana, AAPG Bull., v. 70, p. 1651–1673.

Beaumont, C., Nguyen, M.H., Jamieson, R.A. and Ellis, S., 2006, Crustal flows in large hot orogens, Geological Society, London, Special Publications, 268, p. 91-145.

Bishop, G.A., 1985, Fossil decapod crustaceans from the Gammon ferrugionous member, Pierre Shale (Early Campanian), Black Hills, South Dakota, J. Paleo., v. 59, no.3, p. 605-624.

Boyd, D.W., and Lillegraven, J.A., 2011, Persistence of the Western Interior Seaway: Historical background and significance of ichogenus Rhizocorallium in Paleocene strata, south Central Wyoming, Rocky Mountain Geology, v. 46, p. 43-69.

Cassel, E., J., Breeker, D.O., Henry, C.D., Larson, T.E., and Stockli, D.F., 2014, Profile of a paleo-orogen: High topography across the present-day Basin and Range from 40 to 23 Ma. Geology, v. 42, no 11, p. 1007-1010.

Cather, S.M., 2004, Laramide orogeny in central and northern New Mexico and southern Colorado, in Mack, G.H., and Giles, K.A., eds., The geology of New Mexico, A geologic history: New Mexico Geological Society Special Pub. 11, p. 203-248.

Cerveny, P.F., 1990, Fission-track Thermochronology of the Wind River Range and Other Basement Cored Uplifts in the Rocky Mountain Foreland [Ph.D. dissertation]: Laramie, Wyoming, University of Wyoming, 180 p.

Coney, P.J., and Harms, T.A., 1984, Cordilleran metamorphic core complexes: Cenozoic extensional relics of Mesozoic compression, Geology, v. 12, no. 9, p.550-554.

Copeland, P., Murphy, M.A., Dupré, W.R., and Lapen, T.J., 2011, Oligocene Laramide deformation in southern New Mexico and its implications for Farallon plate geodynamics: Geosphere, v. 7, p.1–11.

Crowell, J.C. 1962, Displacement along the San Andreas fault, California, Geological Society of America Special Paper 71, p.1-58. doi: 10.1130/SPE71-p1.

Davis, G.A., and Lister, G.S. 1988, Detachment faulting in continental extension; perspectives from the southwestern US Cordillera. Geological Society of America Special Papers, 218, 133-160.

De los Santos M.G., Lawton, T.F., Copeland, P., Licht, A., Hall, S.A., 2017, Magnetostratigraphy, age and depositional environment of the Lobo Formation, southwest New Mexico: Implications for the Laramide orogeny in the southern Rocky Mountains, Basin Research, in press

Dickinson, W.R., Klute, M.A., Hayes, M.J., Janecke, S.U., Lundin, E.R., McKittrick, M.A., and Olivares, M.D., 1988, Paleogeographic and paleotectonic setting of Laramide sedimentary basins in the central Rocky Mountain region, GSA Bull., v. 100, p.1023-1039.

Dickinson, W.R., 1991, Tectonic setting of faulted Tertiary strata associated with the Catalina core complex in southern Arizona, Geological Society of America Special Paper 264, p.1-106.

Drewes, H., 1981, Tectonics of southeastern Arizona, USGS Prof. Paper 1144, 96 p.

Eaton, J. G., 1991, Biostratigraphic framework for the Upper Cretaceous rocks of the Kaiparowits Plateau, southern Utah, in Nations, J. D., and Eaton, J. G., eds., Stratigraphy, depositional environments, and sedimentary tectonics of the western margin, Cretaceous Western Interior Seaway, Geological Society of America Special Paper 260, p. 47-63.

Engebretson, D.C., Cox, A., and Thompson, G.A., 1984, Correlation of plate motions with continental tectonics: Laramide to Basin-range, Tectonics, v. 3, p.115-119.

Fan, M., and Carrapa, B., 2014, Late Cretaceous–early Eocene Laramide uplift, exhumation, and basin subsidence in Wyoming: Crustal responses to flat slab subduction: Tectonics, v. 33, p. 509–529

Fan, M., Heller, P.L., Allen, S.D., and Hought, B.G., 2014, Middle Cenozoic uplift and concomitant drying in the central Rocky Mountains and adjacent Great Plains, Geology, v. 42, no. 6, p. 547–550.

Fullsack, P., 1995, An arbitrary Lagrangian-Eulerian formulation for creeping flows and applications in tectonic models: Geophys J Int., v. 120, p. 1-23.

Gill, J.R. and Cobban, W.A., 1966, The Red Bird section of the Upper Cretaceous Pierre Shale in Wyoming, USGS Prof. Paper 393-A, 71 p.

Gill, J.R. and Hail, W.J., 1975, Stratigraphic sections across Upper Cretaceous Mancos Shale-Mesaverde Group boundary, eastern Utah and western Colorado, USGS Oil and Gas Investigation Chart 68.

Gill, J.R., Cobban, W.A., and Schultz, L.G., 1972, Stratigraphy and composition of the Sharon Springs Member of the Pierre Shale in western Kansas, USGS Professional Paper 728, 50 p.

Goldstrand, P.M., 1994, Tectonic development of Upper Cretaceous to Eocene strata of southwestern Utah: GSA Bull., v. 106, p. 145–154.

González-León, C. M., Solari, L., Solé, J., Ducea, M.N., Lawton, T.F., Bernal, J.P., Becuar, E.G., Gray, F., Martínez, M.L., Santacruz, R.L., 2011, Stratigraphy, geochronology, and geochemistry of the Laramide magmatic arc in north-central Sonora, Mexico. Geosphere, v. 7, p., 392-1418.

Hacker, B.R., Abers, G.A., and Peacock, S.M., 2003, Subduction factory 1. Theoretical mineralogy, densities, seismic wave speeds, and H2O contents, J. Geophys. Res., v. 108, p.2029, doi: 10.2029/2002JB002026.

Howard, K.A., and John, B.E., 1987, Crustal extension along a rooted system of imbricate low-angle faults: Colorado River extensional corridor, California and Arizona, Geological Society, London, Special Publications, 28.1, 299-311.

Humphreys, E., Hessler, E., Dueker, K., Farmer, G.L., Erslev, E., and Atwater T., 2003, How Laramide-age hydration of North American lithosphere by the Farallon slab controlled subsequent activity in the western United States, Int. Geol. Rev., v. 45, p. 575-595.

Huntington, K.W., Wernicke, B.P., and Eiler, J.M., 2010, The influence of climate change and uplift on Colorado Plateau paleotemperatures from carbonate ‘‘clumped isotope’’ thermometry, Tectonics, v. 29, p. TC3005, 19 p.

Jacques-Ayala, C., Barth, A.P., Wooden, J.L. & Jacobson, C.E. 2009, Provenance and U-Pb geochronology of the Upper Cretaceous El Chanate Group, northwest Sonora, Mexico, and its tectonic significance. International Geology Review, v. 51, p. 1051-1077.

Jacques-Ayala, C., 1995, Paleogeography and provenance of the Lower Cretaceous Bisbee Broup in the Caborca-Santa Ana area, northwestern Sonora, GSA Special Paper, 301, p.

79-98.

Karato, S.-I. and Wu, P., 1993, Rheology of the upper mantle: A synthesis, Science, v. 260, p. 771-778.

Keith, S.B., and Wilt, J.C., 1986, Laramide orogeny in Arizona and adjacent regions-A strato-tectonic synthesis, in Beatty, B., and Wilkinson, P.A.K., eds., Frontiers in geology and ore deposits of Arizona and the southwest: Arizona Geological Society Digest, v. 16, p. 502-554.

Kelley, S.A., 2005, Low-temperature cooling histories of the Cheyenne Belt and Laramie Peak shear zone, Wyoming, and the Soda Creek–Fish Creek shear zone, Colorado, in Karlstrom, K.E., and Keller, G.R., eds., The Rocky Mountain Region: An evolving lithosphere: American Geophysical Union Geophysical Monograph v. 54, p. 55–70.

Kelley, S.A., 2002, Unroofing of the southern Front Range, Colorado: A view from the Denver Basin, Rocky Mountain Geology, v. 37, p. 189–200.

Kluth, C.F., and Nelson, S.N., 1988, Age of Dawson Arkose, southwestern Air Force Academy, Colorado, and implications for the uplift history of the Front Range, The Mountain Geologist, v. 25, p. 29–35.

Korenaga, J., and W.W. Sager, 2012, Seismic tomography of Shatsky Rise by adaptive importance sampling, J. Geophys. Res., v. 117: B08102, doi: 10.1029/2012JB009248.

Lawton, T.F., 1983, Late Cretaceous fluvial systems and the age of foreland uplifts in central Utah, in Lowell, J.D. ed., Rocky Mountain foreland basins and uplifts: Denver, Colorado, Rocky Mountain Association of Geologists, p. 181–199.

Lehman, T.M., 1991, Sedimentation and tectonism in the Laramide Tornillo Basin of West Texas, Sed. Geol., v. 75, p. 9-28.

Lillegraven, J.A., 2015, Late Laramide tectonic fragmentation of the eastern greater Green River Basin, Wyoming, Rocky Mountain Geology, v. 50, no. 1, p. 30-118.

Lisenbee, A.L., and DeWitt, E., 1993, Laramide evolution of the Black Hills uplift, in Snoke, A.W., Steidtmann, J.R., and Roberts, S.M., eds., Geology of Wyoming, Geological Survey of Wyoming Memoir 5, p. 374–412.

Lopez, J.L. and Steel, R.J., 2015, Laramide signals and architecture of a widespread fluvial sand sheet: Canyon Creek member, southern Wyoming, U.S.A., J. Sed. Res., v. 85, no. 9, p. 1102-1122.

Mederos, S., Tikoff, B., and Bankey, V., 2005, Geometry, timing and continuity of the Rock Springs uplift, Wyoming, and Douglas Creek Arch, Colorado: Implications for uplift mechanisms in the Rocky Mountain foreland, U.S.A., Rocky Mountain Geology, v. 40, p. 167–191.

Mix, H.T., Mulch, A., Kent-Corson, M.L., and Chamberlain, C.P., 2011, Cenozoic migration of topography in the North American Cordillera, Geology, v. 39, p. 87–90.

Molenaar, C.M., 1983, Major depositional cycles and regional correlations of Upper Cretaceous rocks, southern Colorado Plateau and adjacent areas, in Reynolds, M.W., and Dolly, E.D., eds., Mesozoic paleogeography of west central United States: Rocky Mountain Paleogeography Symposium 2: Denver, Colorado, Rocky Mountain Section, Society of Economic Paleontologists and Mineralogists, p. 201–223

Omar, G.I., Lutz, T.M., and Giegengack, R., 1994, Apatite fission-track evidence for Laramide and post-Laramide uplift and anomalous thermal regime at the Beartooth overthrust, Montana-Wyoming, p. GSA Bull., v. 106, p. 74–85.

Peppe D.J., Evans, D.A.D., and Smirnov, A.V., 2009, Magnetostratigraphy of the Ludlow member of the Fort Union Formation (lower Paleocene) in the Williston Basin, North Dakota , GSA Bull., v. 121, p. 65–79.

Price, J.G., and Henry, C.D., 1984, Stress orientations during Oligocene volcanism in Trans-Pecos Texas: Timing the transition from Laramide compression to Basin and Range tension, Geology, v. 12, p. 238-241.

Raynolds, R., G., 2003, Upper Cretaceous and Tertiary stratigraphy of the Denver Basin, Colorado, Rocky Mountain Geology, v. 37, no. 2, p. 111-134.

Tindall, S.E., Storm, L.P., Jenesky, T.A., and Simpson, E.L., 2010, Growth faults in the Kaiparowits Basin, Utah, pinpoint initial Laramide deformation in the western Colorado Plateau, Lithosphere, v. 2, p. 221–231.

Tomlinson, D.W., Copeland, P., Murphy, M.A., and Lapen, T.J., 2013, Oligocene shortening in the Little Burro Mountains, SW New Mexico, Rocky Mountain Geology, v. 48, no. 2, p. 169-183.

Warren, C.J., Beaumont, C., and Jamieson, R.A., 2008, Formation and exhumation of ultra-high-pressure rocks during continental collision: role of detachment in the subduction channel, Geochem. Geophys. Geosys., v. 9:Q04019, doi: 10.1029/2007GC001839.

Wiltschko, D.V., and Dorr, J.A., Jr., 1983, Timing of deformation in overthrust belt and foreland of Idaho, Wyoming, and Utah, AAPG Bull, v. 67, p. 1304-1322.

Zhang, J., Sager, W.W., and Korenaga, J., 2016, The seismic Moho structure of Shatsky Rise oceanic plateau, northwest Pacific Ocean, Earth Planet. Sci. Lett., v. 441, p. 143-154.

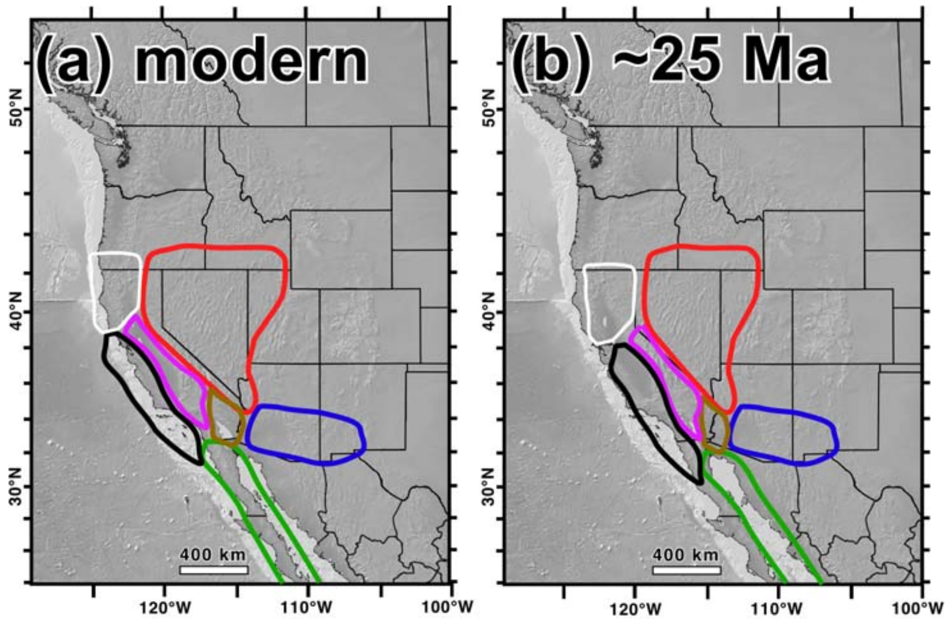

Figure DR1. Illustration of procedures of palinspastic reconstruction. (a) Shapes of areas used in reconstruction in their modern orientation, (b) Shapes of areas used in reconstruction after palinspastic reconstruction. See text for details.

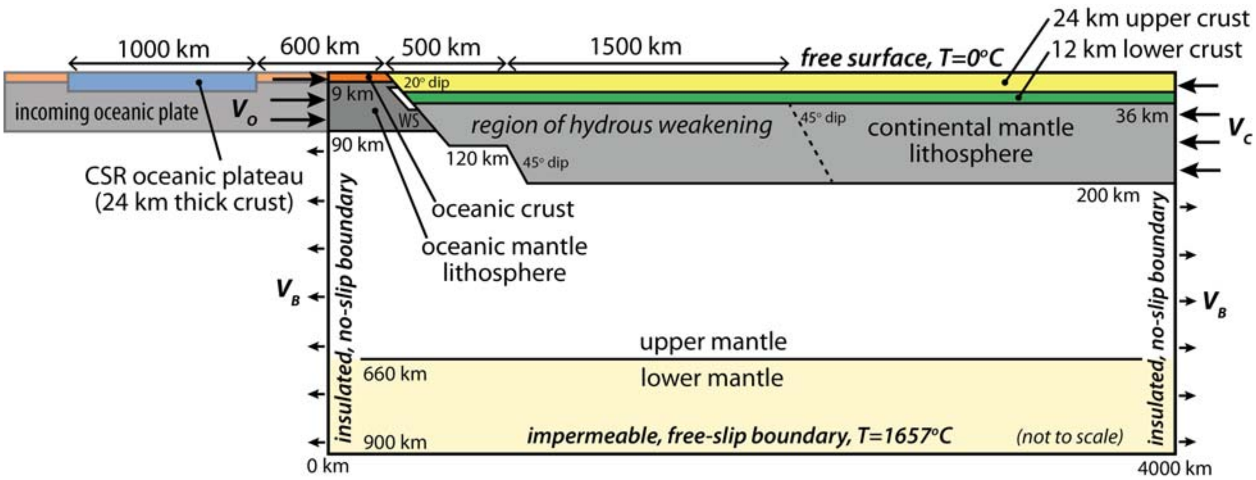

Figure DR2. Initial geometry and boundary conditions of the numerical model. The computational domain is within the 4000 km x 900 km rectangle. The domain is divided into 320 Eulerian finite elements horizontally (12.5 km wide) and 116 elements vertically (3 km height in the upper 60 km, 5 km height at 60-260 km depth, 10 km height at 260-660 km depth and 15 km below 660 km depth). A weak seed (WS) between the continental and oceanic plates aids in subduction initiation. This material is subducted with the oceanic plate and does not affect later model evolution.

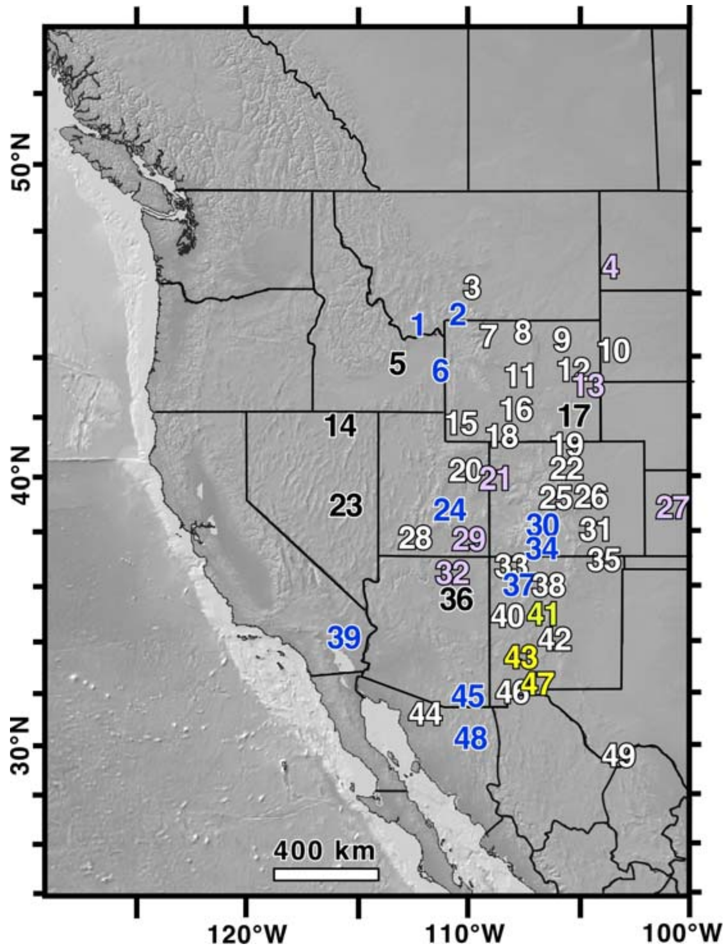

Figure DR3. Map of locations mentioned in Tables DR2-DR5. Lavender numerals represent sites with estimates of the youngest marine sedimentation, black numerals represent sites with estimates of the timing of attainment of maximum surface elevation only, blue numerals represent sites with estimates of the timing of initiation of Laramide deformation only; yellow numerals sites represent sites with estimates of the timing of cessation of Laramide deformation only; white numerals sites represent sites with more than one kind of estimate.

Tables DR1-DR5

Table DR1. Material parameters in geodynamic model.

	Oceanic crust[a]	Oceanic mantle lithosphere	Continental upper crust	Continental lower crust	Cont. mantle lithosphere	Sublithospheric mantle[b]
Plastic rheology[c]						
c_0 (MPa)	0	0	20	0	0	0
ϕ_{eff}	15° to 2°	15°	15° to 2°	15° to 2°	15° to 2°	15° to 2°
Viscous rheology[d]						
f	0.1, 10[a]	5	5	0.1	10	1, 5[b]
B* (Pa $s^{1/n}$)	1.91×10^5	1.92×10^4	2.92×10^6	1.91×10^5	1.92×10^4	1.92×10^4
n	4.7	3.0	4.0	4.7	3.0	3.0
Q (kJ mol^{-1})	485	430	223	485	430	430
V* (cm^3 mol^{-1})	0	10	0	0	10	10
Thermal parameters						
k (W m^{-1} K^{-1})[e]	2.25	2.25	2.25	2.25	2.25	2.25
A (μW m^{-3})	0	0	1.2, 0.9[f]	0.4, 0.2[f]	0	0
c_p (J kg^{-1} K^{-1})	750	1250	750	1250	1250	1250
Density[g]						
ρ_0 (kg m^{-3})	2950	3250	2800	2900	3250	3250
T_0 (°C)	500	1340	500	500	1340	1340
Eclogite ρ_0 (kg m^{-3})	3450	--	--	--	--	--
Eclogite T_0 (°C)	500	--	--	--	--	--
α (K^{-1})	3.0×10^{-5}	3.0×10^{-5}	3.0×10^{-5}	3.0×10^{-5}	3.0×10^{-5}	3.0×10^{-5}

[a] The CSR crust has the same material parameters as the rest of the oceanic crust, except that the CSR crust is 24 km thick and the rheology of the lower 12 km of CSR crust is 10 times stronger. This is needed to prevent the plateau crust from buoyantly detaching from the slab during subduction.

[b] The sublithospheric mantle is disvided into a weak upper mantle (to 660 km depth) and a stronger lower mantle (below 660 km), using different viscous scaling factors (f).

[c] Frictional-plastic deformation follows a Drucker-Prager yield criterion: $J'_2 = c_0\cos\phi_{eff} + P\sin\phi_{eff}$, where where c_0 is the cohesion, ϕ_{eff} is the effective internal angle of friction, and J'_2 is the square root of the second invariant of the deviatoric stress tensor. Strain softening is included through a linear decrease in ϕ_{eff} over accumulated stain of 0.5 to 1.5.

[d] The effective viscosity (η_{eff}) for viscous deformation is given by: $\eta_{eff} = f(B^*)(\dot{I}_2)^{(1-n)/n}\exp\left(\frac{E^*+PV^*}{nRT}\right)$, where $\dot{I}_2$ is the square root of the second invariant of the strain rate tensor, P is the total pressure, T is the temperature, f is a scaling factor, B^* is the pre-exponential factor, n is the stress exponent, E^* is the activation energy, V^* is the activation volume and R is the universal gas constant.

[e] thermal conductivity (k) at temperatures less than 1390ºC; at higher temperatures, thermal conductivity increases linearly from 2.25 W m^{-1} K^{-1} at 1390ºC to 52.75 W m^{-1} K^{-1} at 1430ºC.

[f] the first A corresponds to crustal heat production for the 120 km thick lithosphere (Fig. DR4); the second A is for the 200 km thick lithosphere.

[g] density varies with temperature: $\rho(T) = \rho_0(1-\alpha(T-T_0))$, where ρ_0 is the reference density at temperature T_0 and α is the volumetric thermal expansion coefficient.

Table DR 2. Estimates for the age of youngest marine strata

Location	Age of youngest marine strata (Ma)	Type of data	reference	Distance along A-A' in Fig. 1 (km)	Location on Fig. DR3
San Juan Basin	76	stratigraphic	Cather, 2004	950	33
Piceance Basin,	79	stratigraphic	Gill and Hail, 1975	1100	21
Wind River Basin, central WY	73	stratigraphic	Dickinson et al., 1988	1400	11
North Park Basin, northern CO	75	stratigraphic	Dickinson et al., 1988	1500	19
Middle Park Basin, northern CO	73	stratigraphic	Dickinson et al., 1988	1430	22
South Park Basin, northern CO	73	stratigraphic	Dickinson et al., 1988	1340	25
Raton Basin, NE NM	72	stratigraphic	Cather, 2004	1240	35
Powder River Basin, NE WY	68	stratigraphic	Dickinson et al., 1988	1730	12
Sierra Blanca Basin, central NM	88	stratigraphic	Cather, 2004	980	42
Gallisto Basin, northern NM	84	stratigraphic	Dickinson et al., 1988, Cather, 2004	1020	37
Washakie Basin, southern WY- NW CO	70	stratigraphic	Dickinson et al., 1988	1300	18
Huerfano Park Basin, southern CO	75	stratigraphic	Dickinson et al., 1988	1340	31
Uinta Basin, eastern UT	82	stratigraphic	Dickinson et al., 1988	1100	20
Big Bend region, west TX	80	stratigraphic	Lehman, 1991	800	49
Northern Sonora	100	stratigraphic	Jacques-Ayala, C., 1995	390	44
Western Kansasa	69	stratigraphic	Gill et al., 1972	1640	27
Black Hills, SD	70	stratigraphic	Bishop, 1985	1900	10
Eastern Wyoming	69	stratigraphic	Gill and Cobban, 1966	1690	13
Little Hatchets Mtns, SW NM	97	stratigraphic	Clinkscales and Lawton, 2012	725	46
Crazy Mountains	72	stratigraphic	Dickinson et al., 1988	1500	3
Baca Basin	89	stratigraphic	Cather, 2004	860	40
Carthage Basin	88	stratigraphic	Cather, 2004	920	49
Big Horn Basin	75	stratigraphic	Dickinson et al., 1988	1550	7
Williston Basin, SW ND	64	stratigraphic	Peppe et al., 2009	2050	4
Hanna Basin	63	stratigraphic	Boyd and Lillegraven, 2011	1450	16
Denver Basin	69	stratigraphic	Raynolds, 2003	1460	26
Black Mesa Basin	84	stratigraphic	Molenaar, 1983	800	32
SE Utah	90	stratigraphic	Eaton, 1991	930	29
N. Kaiparowits Plateau, SW UT	84	stratigraphic	Eaton, 1991	725	28

Table DR3. Estimates for the time of initiation of Laramide deformation

Location	Approximate time of initiation of Laramide deformation (Ma)	Type of data	reference	Distance along A-A' in Fig. 1 (km)	Location on Fig. DR3
NE Sonora	93	stratigraphic and structural	González-León, *et al.,* 2011	420	48
NW Sonora	91	stratigraphic and structural	Jacques-Ayala et al., 2009	390	44
SE California	85	structural and geochemical	Keith and Wilt, 1986	320	39
N. Kaiparowits Plateau, SW UT	80	stratigraphic and structural	Heller and Liu, 2016; Goldstrand, 1994; Tindall et al., 2010	725	28
Madison-Gravelly uplift	79	stratigraphic	Perry et al., 1990	1380	1
Hanna Basin, central WY	79	stratigraphic	Heller and Liu, 2016, Kelly, 2005; Lillegraven, 2015	1450	16
San Juan Basin, NW NM	78	stratigraphic	Heller and Liu, 2016; Cather, 2004	950	33
Archuleta Anticlinorium	78 - 75	structural	Cather, 2004	1100	34
Crazy Mountains Basin, southern MT	77	stratigraphic	Dickinson et al., 1988	1500	3
Green River Basin, SW WY	76 - 73	stratigraphic	Heller and Liu, 2016; Mederos et al., 2005; Lopez and Steel, 2015	1220	15
Ancestral Teton-Gros Ventre uplift	73	structural	Wiltschko and Dorr, 1983	1350	6
Nacimiento Uplift	~75	stratigraphic	Cather, 2004	1000	37
Uinta Basin, eastern UT	75	stratigraphic	Heller and Liu, 2016, Lawton, 1983	1100	20
SE Arizona	80 - 75	stratigraphic, structural	Drewes, 1981	570	45
San Rafael Swell, southern Utah	73	stratigraphic	Lawton, 1983	930	24
San Juan uplift	72	structural	Cather, 2004	1110	30
Little Hatchet Mountains	75	structural	Clinkscales and Lawton, 2012	725	46
Raton Basin, NE NM	71	stratigraphic	Cather, 2004	1240	35
Denver Basin, eastern CO	71	stratigraphic, Thermochronologic	Heller and Liu, 2016, Kelley, 2002; Kluth and Nelson, 1988	1460	26
Wind River Basin, central WY	70	stratigraphic	Dickinson et al., 1988	1400	11
Big Horn Mountains, northwest WY	68	Thermochronologic	Cervany, 1990	1560	8
South Park Basin, central CO	68	stratigraphic	Dickinson et al., 1988	1340	25
Huerfano Park Basin, southern CO	68	stratigraphic	Dickinson et al., 1988	1340	31
South Powder River Basin, eastern WY	68	stratigraphic	Heller and Liu, 2016	1650	12
Middle Park Basin, northern CO	67	stratigraphic	Dickinson et al., 1988	1430	22
Washakie Basin, southern WY-NW CO	66	stratigraphic	Dickinson et al., 1988	1300	18
Gallisto Basin, northern NM	66	stratigraphic	Dickinson et al., 1988	1020	37
North Powder River Basin, eastern WY	66	stratigraphic	Heller and Liu, 2016, Ayers, 1986	1720	12
North Park Basin, northern CO	65	stratigraphic	Dickinson et al., 1988	1500	19
Beartooth Mountains, SW MT	61	Thermochronologic	Omar et al., 1994	1580	2
Black Hills, western SD	60	structural	Heller and Liu, 2016, Lisenbee and DeWitt, 1993	1830	10

Table DR4. Estimates for the time of cessation of Laramide deformation

Location	Approximate time of cessation of Laramide deformation (Ma)	Type of data	reference	Distance along A-A' in Fig. 1 (km)	Location on Fig. DR3
Crazy Mountains Basin, southern MT	58 - 55	stratigraphic	Dickinson et al., 1988	1500	3
Big Horn Basin, northwest WY	52 - 50	stratigraphic	Dickinson et al., 1988	1550	7
Wind River Basin, central WY	52 - 50	stratigraphic	Dickinson et al., 1988	1400	11
San Juan Basin	55-50	stratigraphic	Cather, 2004	950	33
North Park Basin, northern CO	52 - 35	stratigraphic	Dickinson et al., 1988	1500	19
Middle Park Basin, northern CO	52 - 35	stratigraphic	Dickinson et al., 1988	1430	22
Florida Mountains, SW NM	52-40	stratigraphic	De los Santos et al., 2017	770	47
South Park Basin, northern CO	52 - 36	stratigraphic	Dickinson et al., 1988	1340	25
Raton Basin, NE NM	53-49	stratigraphic	Cather, 2004	1240	35
Powder River Basin, NE WY	50 - 35	stratigraphic	Dickinson et al., 1988	1720	12
Green River Basin, SW WY	48 - 29	stratigraphic	Dickinson et al., 1988	1220	15
N. Kaiparowits Plateau, SW UT	48-42	stratigraphic	Goldstrand, 1994	725	28
Sierra Blanca Basin, central NM	41	stratigraphic	Cather, 2004	980	41
Carthage-La Joya Basin, central NM	39	stratigraphic	Cather, 2004	920	42
Gallisto Basin, northern NM	39-36	stratigraphic	Dickinson et al., 1988; Cather, 2004	1020	37
Washakie Basin, southern WY- NW CO	38 - 29	stratigraphic	Dickinson et al., 1988	1300	18
Huerfano Park Basin, southern CO	36 - 35	stratigraphic	Dickinson et al., 1988	1320	31
Uinta Basin, eastern UT	35 - 29	stratigraphic	Dickinson et al., 1988	1100	20
Baca Basin, western NM	33	stratigraphic	Cather, 2004	860	40
Big Bend region, west TX	32	structural	Price and Henry, 1984	800	49
Silver City region, SW NM	29	structural	Copeland et al., 2011; Tomlinson et al., 2013	710	43

418 **Table DR5.** Estimates for the time of attainment of maximum surface elevation.

Location	Approximate time of attainment of maximum surface elevation (Ma)	Type of data	reference	Distance along A-A' in Fig. 1 (km)	Location on Fig. DR3
Big Horn Mountains	57	O isotopes, stratigraphic, thermochronologic	Fan and Carrapa, 2014	1620	8
Washakie Range	53	O isotopes	Fan and Carrapa, 2014	1290	18
Uinta Mountains	49	O isotopes	Fan and Carrapa, 2014	1080	20
Wind River Range	47	O isotopes	Fan and Carrapa, 2014	1490	11
SE Wyoming	40	O isotopes	Fan et al., 2014	1580	17
Southern Idaho	40	O isotopes	Chamberlain et al., 2012; Mix et al., 2011	1180	5
NE Nevada	37	O isotopes	Chamberlain et al., 2012; Mix et al., 2011	820	14
Southern Nevada	30	O isotopes	Chamberlain et al., 2012; Mix et al., 2011, Cassel et al., 2014	650	23
NE Arizona	20	O isotopes	Huntington et al., 2010	720	36